Supporting Information

Machine Learning Boosted Design of Ionic Liquids for CO_2 Absorption and Experimental Verification

Nahoko Kuroki[1,2], Yuki Suzuki[3], Daisuke Kodama[3*], Firoz Alam Chowdhury[4], Hidetaka Yamada[4,5], Hirotoshi Mori[1*]*

[1] Department of Applied Chemistry, Faculty of Science and Engineering, Chuo University, 1-13-27 Kasuga, Bunkyo-ku, Tokyo 112-8551, Japan

[2] Japan Science and Technology Agency, ACT-X, 4-1-8 Honcho, Kawaguchi, Saitama 332-0012, Japan

[3] Department of Chemical Biology and Applied Chemistry, College of Engineering, Nihon University, 1 Nakagawara, Tokusada, Tamura-machi, Koriyama, Fukushima 963-8642, Japan

[4] Research Institute of Innovative Technology for the Earth, 9-2 Kizugawadai, Kizugawa, Kyoto 619-0292, Japan

[5] Frontier Science and Social Co-creation Initiative, Kanazawa University, Kakuma-machi, Kanazawa, Ishikawa 920-1192, Japan

* Corresponding authors:

kuroki.91d@g.chuo-u.ac.jp (N. Kuroki),
kodama.daisuke@nihon-u.ac.jp (D. Kodama),
qc-forest.19d@g.chuo-u.ac.jp (H. Mori).

Supporting Methods

1. Chemical space and features for machine learning S3

2. Synthesis S6

3. Measurements S9

Supporting Results S11

Supporting References S23

Supporting Methods

1. Chemical space and features for machine learning

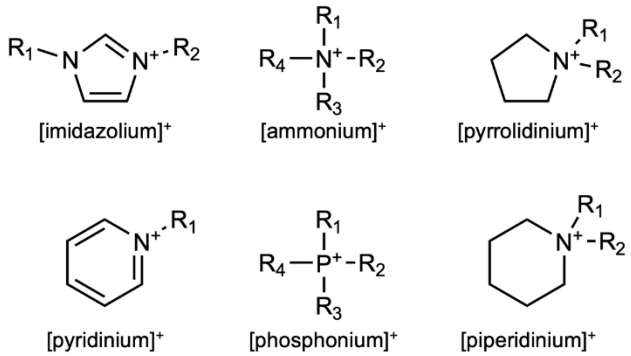

Figure S1. General structures of the cations.

Table S1. List of anions.

Class	Structures
Fluorine-inorganic	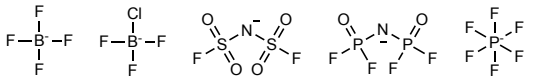
Nonfluorine-inorganic	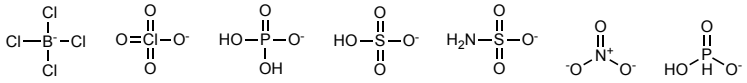
Fluorine-organic	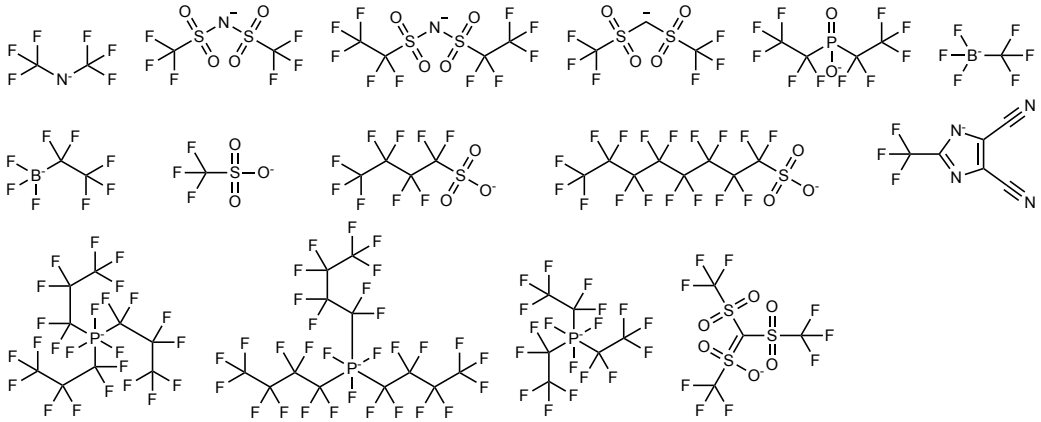
Nonfluorine-organic	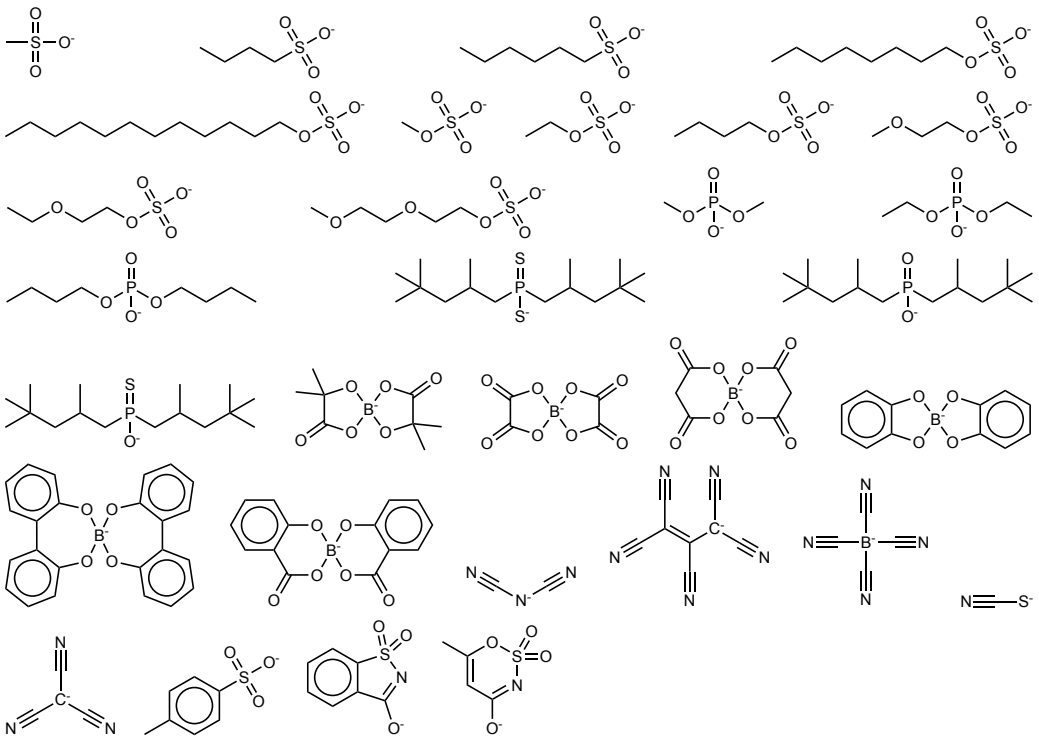

Table S2. Features used.

Class	Feature			Symbol
Geometric	Volume			V
	Surface area			A
	Molecular weight			MW
	Number of conformers			N_{conf}
Electronic	$M_i = \int p(\sigma) f_i(\sigma) d\sigma$ [a]		$f_i(\sigma)$	
	σ-moments			
		2nd	σ^2	M_2
		3rd	σ^3	M_3
		4th	σ^4	M_4
		5th	σ^5	M_5
		6th	σ^6	M_6
	Hydrogen bonding (HB) moments[b]			
		acceptor	$\begin{cases} 0 & (+\sigma \le \sigma_{\text{HB}}) \\ \sigma + \sigma_{\text{HB}} & (+\sigma > \sigma_{\text{HB}}) \end{cases}$	$M_{\text{HB}acc}$
		donor	$\begin{cases} 0 & (-\sigma \le \sigma_{\text{HB}}) \\ \sigma - \sigma_{\text{HB}} & (-\sigma > \sigma_{\text{HB}}) \end{cases}$	$M_{\text{HB}don}$

a) $p(\sigma)$: σ-profile, which represents surface charge density distribution, σ.
b) A threshold of $\sigma_{\text{HB}} = 0.1$ was used.

2. Synthesis

The chemicals used in this study are listed in **Table S3**. The detailed synthesis procedures for $[P_{66614}][A]$ (A = TFSA, PFOS, and PF_6) were as follows.

$[P_{66614}][TFSA]$.[1] $[P_{66614}][Cl]$ (25 g, 48.1 mmol) was dissolved in CH_2Cl_2 (150 mL). An aqueous solution of Li[TFSA] (16.7 g, 58.2 mmol, 50 mL) was added dropwise. The reaction mixture was stirred for 12 h at room temperature. Then, CH_2Cl_2 (100 mL) and water (150 mL) were added, and the separated organic layer was washed with water until the aqueous layer produced no precipitation in the silver nitrate test. CH_2Cl_2 was removed using a rotary evaporator under reduced pressure. The obtained product was dried under vacuum at 333 K to yield a light-yellow viscous liquid (35.7 g, 97 mol%).

$[P_{66614}][PFOS]$.[2] $[P_{66614}][Cl]$ (25 g, 48.1 mmol) was dissolved in CH_2Cl_2 (150 mL). An aqueous solution of K[PFOS] (31.4 g, 58.2 mmol, 50 mL) was added dropwise. The reaction mixture was stirred for 16 h at room temperature. Then, CH_2Cl_2 (100 mL) and water (150 mL) were added, and the separated organic layer was washed with water until a neutral pH was obtained in the water wash. CH_2Cl_2 was removed using a rotary evaporator under reduced pressure. The obtained product was dried under vacuum at 333 K to yield a pale-yellow viscous liquid (45.2 g, 96 mol%).

$[P_{66614}][PF_6]$.[1] $[P_{66614}][Cl]$ (25 g, 48.1 mmol) was dissolved in CH_2Cl_2 (150 mL). An aqueous solution of Li[PF_6] (8.84 g, 58.2 mmol, 50 mL) was added dropwise. The reaction mixture was stirred for 12 h at room temperature. Then, CH_2Cl_2 (100 mL) and water (150 mL) were added, and the separated organic layer was washed with water until the aqueous layer produced no precipitation in the silver nitrate test. CH_2Cl_2 was removed using a rotary evaporator under reduced pressure. The obtained product was dried under vacuum at 333 K to yield a pale-yellow viscous liquid (29.5 g, 97 mol%).

The obtained ILs were further dried under vacuum for 72 h at 343 K before measurements. The ILs were identified with liquid chromatography/electrospray ionization-mass spectrometry (LC/ESI-MS: Waters, 2695/ZQ2000) (**Figure S2**). The water content of the ILs was determined by Karl–Fischer titration (Kyoto Electronics Manufacturing Co., Ltd., MKC-520), resulting in 67, 116, and 156 ppm for $[P_{66614}][A]$ with A = TFSA, PFOS, and PF_6, respectively.

Table S3. Chemicals used in this study.

Chemical	CASRN®	Source	Purity	Analysis method
$[P_{66614}][TFSA]$ trihexyl(tetradecyl)phosphonium bis(trifluoromethanesulfonyl)amide	460092-03-9	Synthesized	>97 mol%	LC/ESI-MS
$[P_{66614}][PFOS]$ trihexyl(tetradecyl)phosphonium perfluorooctanesulfonate		Synthesized	>96 mol%	LC/ESI-MS
$[P_{66614}][PF_6]$ trihexyl(tetradecyl)phosphonium hexafluorophosphate	374683-44-0	Synthesized	>97 mol%	LC/ESI-MS
$[P_{66614}][Cl]$ trihexyl(tetradecyl)phosphonium chloride	258864-54-9	Tokyo Chemical Industry Co., Ltd.	>97 mol%	Volumetric analysis
Li[TFSA] lithium bis(trifluoromethanesulfonyl)amide	90076-65-6	Tokyo Chemical Industry Co., Ltd.	>98 mol%	Volumetric analysis
K[PFOS] potassium heptadecafluorooctane-1-sulphonate	2795-39-3	Sigma-Aldrich	>98 mol%	Volumetric analysis
$Li[PF_6]$ lithium hexafluorophosphate	21324-40-3	Tokyo Chemical Industry Co., Ltd.	>97 mol%	Volumetric analysis
CH_2Cl_2 dichloromethane	75-09-2	FUJIFILM Wako Pure Chemical Corporation	>99.5 mass%	Gas chromatography
CO_2 carbon dioxide	124-38-9	Showa Denko Gas Products Co., Ltd.	>99.999 vol%	Gas chromatography

[P_{66614}][TFSA]

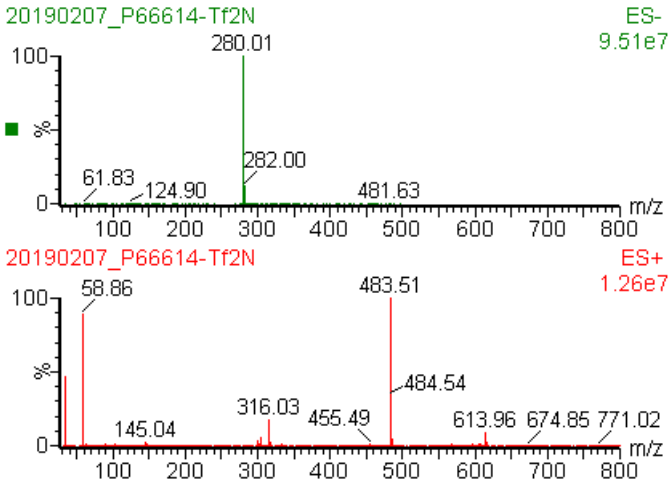

[P_{66614}][PFOS]

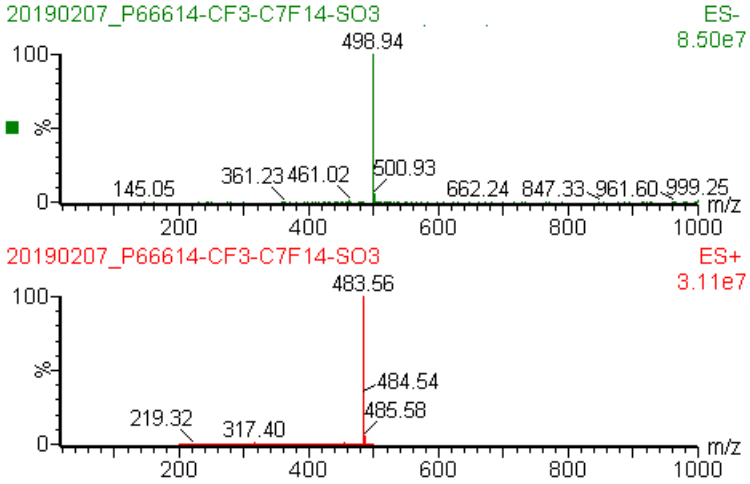

[P_{66614}][PF_6]

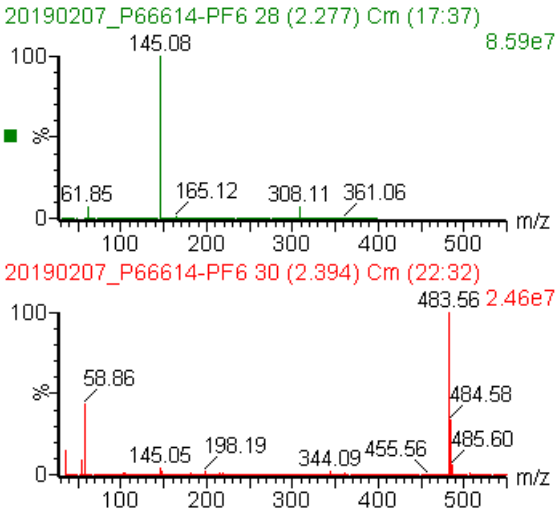

Figure S2. LC/ESI-MS spectra of [P_{66614}][A] (A = TFSA, PFOS, and PF_6).

3. Measurements

- **Atmospheric pressure**

The experimental apparatuses for the density and viscosity measurements were the same as those used in our previous studies.[3-5] The density of an IL was determined using a vibrating tube densimeter (Anton Paar, DMA 5000M). The instrumental constants were calibrated with dry air and Milli-Q water (Millipore Direct-Q3 UV). The viscosity of an IL was measured using a rotating-cylinder viscometer (Anton Paar, Stabinger SVM 3000) equipped with a built-in densimeter. We confirmed the validity of the viscometer readings using reference samples (S60, N100, and S200) supplied by the Cannon Instrument Company. The samples were transferred to a gastight syringe under a dry nitrogen atmosphere (dew point less than 243 K) and injected into the instrument without contacting moisture. The expanded uncertainties for the densities and viscosities were 0.05 $kg \cdot m^{-3}$ and <2%, respectively.

- **High pressure**

The experimental apparatus for the high-pressure density measurement was the same as that used in our previous studies.[6,7] The high-pressure density of an IL was measured using a vibrating tube densimeter (Anton Paar, DMA HP). The pressure was generated with a syringe pump (Nova Swiss, 550.0202.1) and measured by a pressure gauge (Druck, PDCR 911) with a pressure indicator (Druck DPI 145). The standard uncertainties in the temperature, pressure, and density were 0.01 K, 0.006 MPa, and 0.2 $kg \cdot m^{-3}$, respectively. The instrumental constants were calibrated at 298.15−353.15 K with helium, ultrapure water (Millipore Direct-Q 3 UV), and toluene up to 50 MPa, and with carbon tetrachloride at atmospheric pressure. The high-pressure densities of $[P_{66614}][A]$ (A = TFSA and PFOS) and $[P_{66614}][PF_6]$ were measured at 313.15−353.15 K and 323.15−353.15 K, respectively, up to 50 MPa.

3.3 Equations used

Quadratic equation	$\rho = a + bT + cT^2$
Arrhenius equation	$\eta = A\exp\left(\frac{E_a}{RT}\right)$
Vogel–Fulcher–Tammann (VFT) equation	$\eta = A\exp\left(\frac{B}{T - T_0}\right)$

Equation of state (EoS)	
Tait[8]	$v_{\mathrm{IL}} = \frac{1}{\rho} = \frac{1}{\rho_0}\left\{1 - \mathrm{C}\ln\left(1 + \frac{p}{B}\right)\right\}$ $\rho_0 = a_0 + a_1 T + a_2 T^2,\ B = b_0\exp(-b_1 T)$
Sanchez–Lacombe[9,10]	$\tilde{\rho}^2 + \tilde{p} + \tilde{T}\left\{\ln(1 - \tilde{\rho}) + \left(1 - \frac{1}{r}\right)\tilde{\rho}\right\} = 0$ $\left(\tilde{p} = \frac{p}{p^*},\ \tilde{T} = \frac{T}{T^*},\ r = \frac{Mp^*}{RT^*\rho^*}\right)$

Average relative deviation (ARD)	$ARD\% = \frac{100}{\#\mathrm{data}}\sum\frac{\lvert(\mathrm{exp.value}) - (\mathrm{calc.value})\rvert}{(\mathrm{exp.value})}$

ρ: Density, η: Viscosity, p: Pressure, T: Temperature, R: Gas constant, E_a: Activation energy, v_{IL}: Specific volume, $\{A\text{-}C,\ a_i,\ b_i\}$: Constants. Asterisk and tilde indicate critical parameters and reduced properties, respectively.

Supporting Results

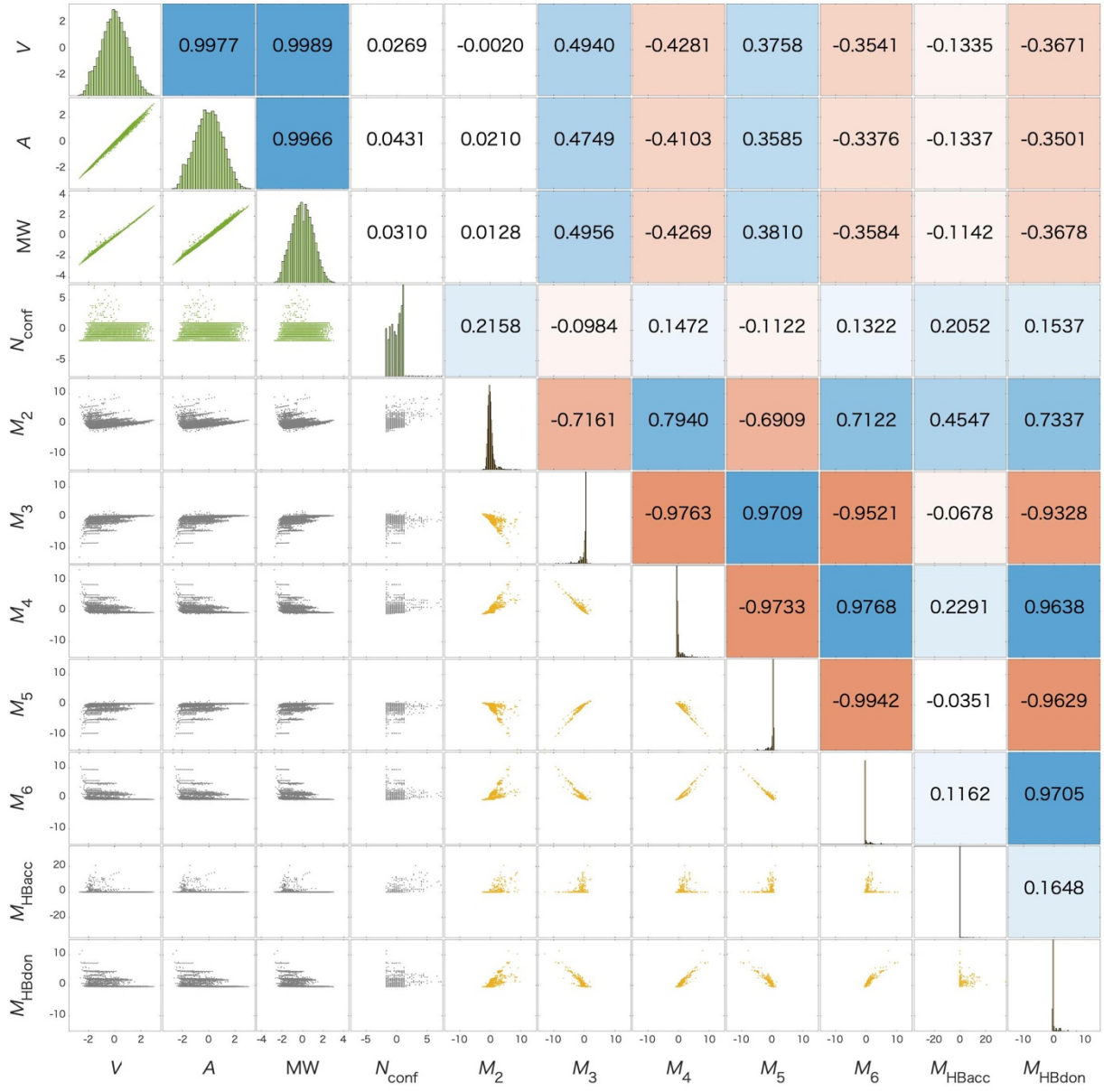

Figure S3. The correlation matrix of cation features. Upper and lower triangles show the correlation coefficients and bivariate scatter plots, respectively. The diagonal shows the distribution of each feature.

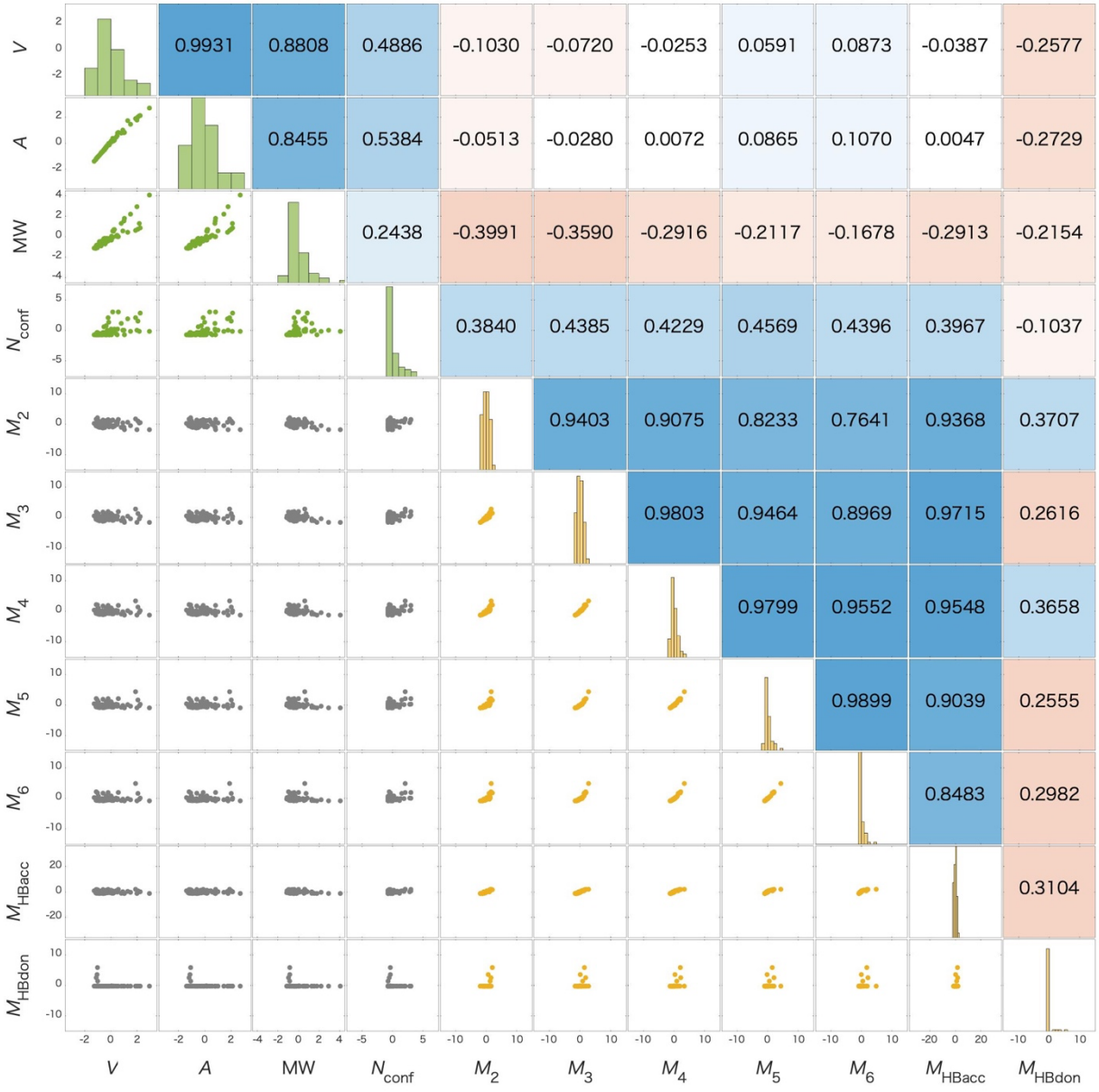

Figure S4. The correlation matrix of anion features. Upper and lower triangles show the correlation coefficients and bivariate scatter plots, respectively. The diagonal shows the distribution of each feature.

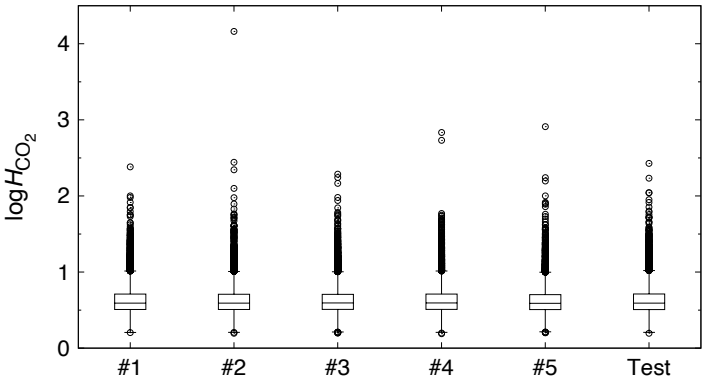

Figure S5. The distribution of training (#1−5) and test data sets. Each set includes 10,000 ILs randomly selected from the total 402,114 candidates.

Table S4. Change in the coefficient of determination for each trained model optimized by the wrapper method. The numbers of features are doubled with respect to the wrapper cycle because ILs consist of a cation–anion pair. The order of the features is sorted to achieve the highest performance in each wrapper cycle. The data in bold numerals are depicted in **Figure 2**(a).

Cycle (# Features)	1 (2)	2 (4)	3 (6)	4 (8)	5 (10)	6 (12)	7 (14)	8 (16)	9 (18)	10 (20)	11 (22)
V	**0.38**										
M_2	0.24	**0.84**									
MW	0.54	0.46	**0.88**								
M_5	0.17	0.39	0.74	**0.89**							
M_6	<0	<0	0.73	0.90	**0.91**						
A	0.54	0.38	0.79	0.87	0.87	**0.91**					
M_3	0.26	0.58	0.81	0.88	0.89	0.89	**0.92**				
M_4	0.23	0.61	0.87	0.90	0.82	0.85	0.89	**0.91**			
N_{conf}	0.01	0.31	0.77	0.84	0.83	0.88	0.90	0.91	**0.91**		
M_{HBdon}	0.24	0.07	0.35	0.82	0.85	0.86	0.89	0.91	0.89	**0.89**	
M_{HBacc}	0.06	0.22	0.87	0.92	0.91	0.89	0.91	0.92	0.90	0.90	**0.90**

Table S5. Change in the root mean square error for each trained model optimized by the wrapper method. The numbers of features are doubled with respect to the wrapper cycle because ILs consist of a cation–anion pair. The order of the features is sorted to achieve the highest performance in each wrapper cycle. The data in bold numerals are depicted in **Figure 2**(a).

Cycle (# Features)	1 (2)	2 (4)	3 (6)	4 (8)	5 (10)	6 (12)	7 (14)	8 (16)	9 (18)	10 (20)	11 (22)
V	**3.67**										
M_2	4.38	**1.84**									
MW	3.40	3.38	**1.68**								
M_5	4.56	3.85	2.42	**1.56**							
M_6	16.07	19.71	2.33	1.60	**1.54**						
A	3.34	3.59	2.04	1.72	1.71	**1.48**					
M_3	4.32	3.24	2.12	1.70	1.63	1.64	**1.40**				
M_4	4.40	3.08	1.77	1.60	2.05	1.91	1.66	**1.50**			
N_{conf}	4.98	3.76	2.30	1.87	1.84	1.70	1.60	1.49	**1.47**		
M_{HBdon}	4.36	4.31	3.63	2.05	1.96	1.88	1.68	1.52	1.68	**1.65**	
M_{HBacc}	4.86	3.96	1.75	1.39	1.48	1.66	1.53	1.38	1.57	1.58	**1.54**

Table S6. Change in the mean absolute error for each trained model optimized by the wrapper method. The numbers of features are doubled with respect to the wrapper cycle because ILs consist of a cation–anion pair. The order of the features is sorted to achieve the highest performance in each wrapper cycle. The data in bold numerals are depicted in **Figure 2**(a).

Cycle (# Features)	1 (2)	2 (4)	3 (6)	4 (8)	5 (10)	6 (12)	7 (14)	8 (16)	9 (18)	10 (20)	11 (22)
V	**0.481**										
M_2	1.445	**0.189**									
MW	0.564	0.439	**0.163**								
M_5	1.262	0.400	0.180	**0.146**							
M_6	1.388	0.523	0.184	0.148	**0.138**						
A	0.610	0.405	0.186	0.153	0.140	**0.130**					
M_3	1.163	0.375	0.177	0.152	0.138	0.136	**0.123**				
M_4	1.231	0.333	0.177	0.148	0.159	0.145	0.129	**0.122**			
N_{conf}	1.691	0.441	0.202	0.164	0.149	0.143	0.130	0.124	**0.122**		
M_{HBdon}	1.363	0.390	0.198	0.160	0.149	0.145	0.126	0.121	0.120	**0.117**	
M_{HBacc}	1.602	0.460	0.190	0.148	0.144	0.143	0.135	0.122	0.126	0.126	**0.115**

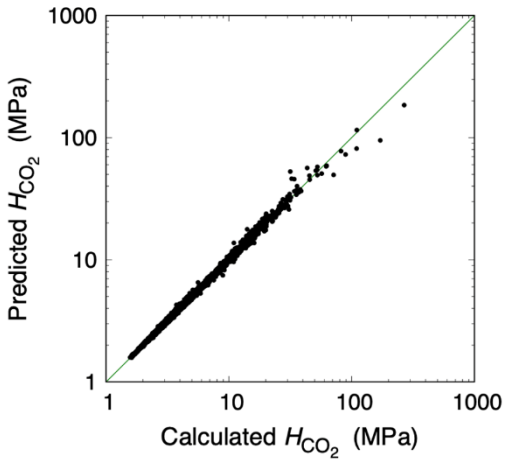

Figure S6. Correlation between Henry's law constants predicted by the Gaussian process regression model (machine learning) and calculated by COSMO-RS (statistical thermodynamics calculation) for 10,000 randomly selected entries of the test data not used to train the model.

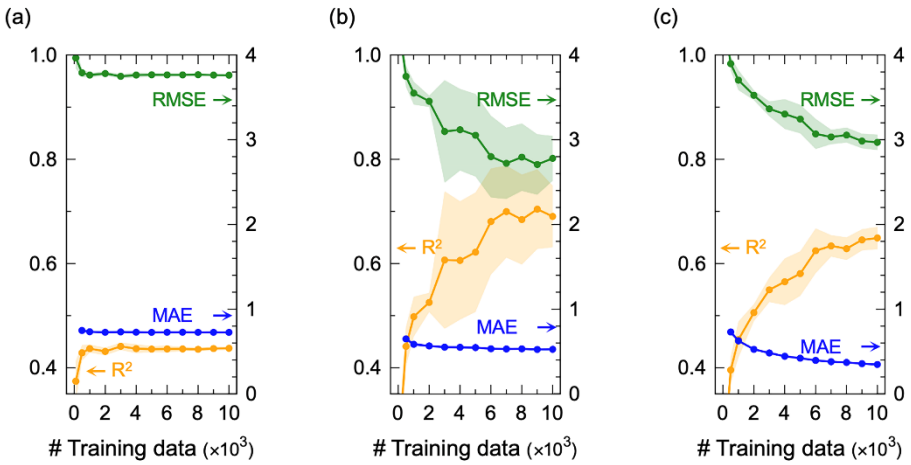

Figure S7. Learning curves for the test data not used to train the model with respect to the number of features. (a) Linear, (b) XGBoost, and (c) random forest regression were used to create the models. V, M_2, MW, M_5, M_6, and A were used for the features. For (a), ordinary least squares regression was applied without robust fitting. For (b) and (c), 30 ensemble learning cycles were trained with 0.1 learning rate for shrinkage.

Table S7. Predicted Henry's law constants H_{CO2} (MPa) for phosphonium-based ILs ([P_{66614}][A]).

	H_{CO2}
Tris(nonafluorobutyl)trifluorophosphate	1.79
Tris(perfluoropropyl)trifluorophosphate	1.91
Tris(pentafluoroethyl)trifluorophosphate	2.09
Bis(biphenyl-2,2'-diylbisoxy)borate	2.50
Bis(2,4,4-trimethylpentyl)dithiophosphinate	2.65
Pentafluoroethyltrifluoroborate	2.76
Bis(pentafluoroethylsulfonyl)amide	2.76
Perfluorooctanesulfonate (PFOS)	2.78
Tris(trifluoromethanesulfonyl)methide	2.81
Tetrachloroborate	2.82
Bis(2,4,4-trimethylpentyl)thiophosphinate	2.86
Bis(pentafluoroethyl)phosphinate	2.87
Bis(trifluoromethyl)amide	2.89
Trifluoro(trifluoromethyl)borate	2.90
Hexafluorophosphate (PF_6)	2.91
Trifluoromethyltrifluoroborate	3.03
Perfluorobutanesulfonate	3.05
Bis(trifluoromethanesulfonyl)amide (TFSA)	3.06

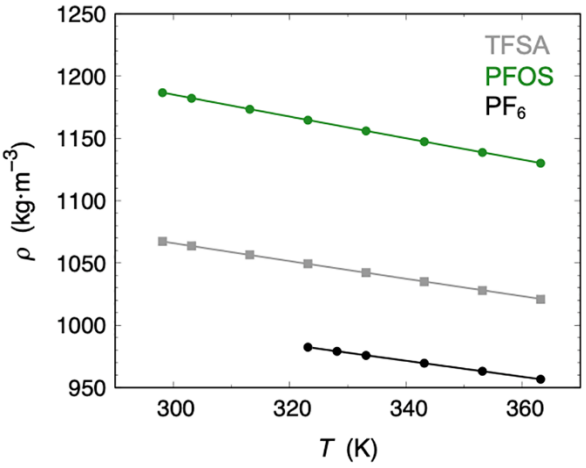

Figure S8. Density of $[P_{66614}][A]$ (A = TFSA, PFOS, and PF_6) at atmospheric pressure. The solid lines represent fits by a quadratic equation.

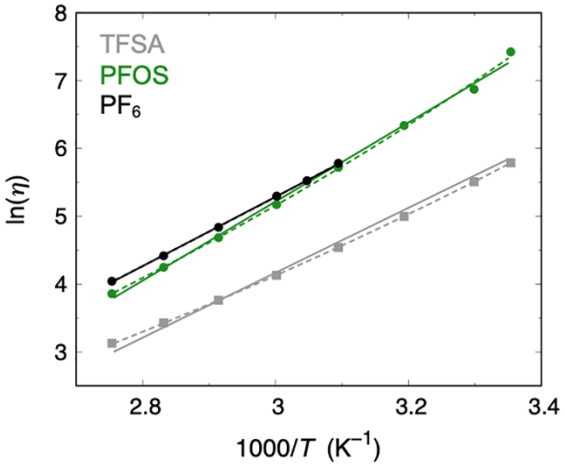

Figure S9. Viscosity of $[P_{66614}][A]$ (A = TFSA, PFOS, and PF_6) at atmospheric pressure. The solid and dashed lines represent fits using the Arrhenius and VFT equations, respectively.

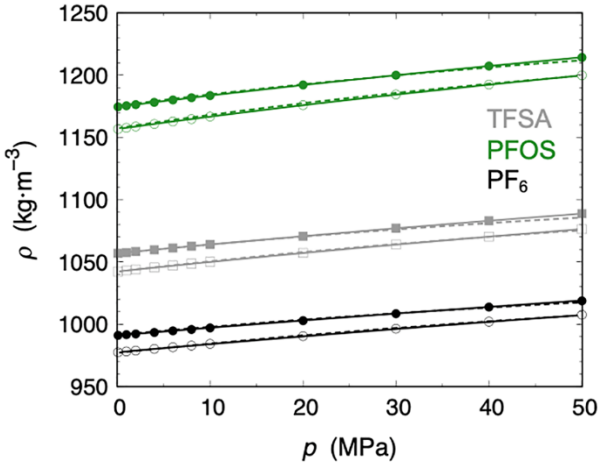

Figure S10. High-pressure density of $[P_{66614}][A]$ (A = TFSA, PFOS, and PF_6). Data at 313.15 and 333.15 K are indicated by closed and opened points, respectively. (**Solid line**: Tait equation, **dashed line**: Sanchez–Lacombe equation.)

Table S8. Density ρ (kg·m^{-3}) and viscosity η (mPa·s) of [P_{66614}][A] (A = TFSA, PFOS, and PF_6) at atmospheric pressure. Standard uncertainties of temperature were 0.01 K. Relative expanded uncertainties for density and viscosity were 0.004 and 0.02, respectively (average of 10 measurements).

	TFSA		PFOS		PF_6	
T	ρ	η	ρ	η	ρ	η
298.15	1067.32	326.6	1186.74	1675.8	–	–
303.15	1063.70	246.9	1182.29	964.5	–	–
313.15	1056.53	147.9	1173.36	565.9	–	–
323.15	1049.38	93.6	1164.69	304.8	982.42	324.3
328.15	–	–	–	–	979.20	250.9
333.15	1042.22	62.1	1156.04	176.2	975.81	199.7
343.15	1035.08	43.0	1147.39	108.1	969.56	126.0
353.15	1027.93	30.8	1138.76	69.92	963.12	82.90
363.15	1020.81	22.8	1130.14	47.31	956.67	56.91

Table S9. Coefficients of the best fits for quadratic, Arrhenius, and VFT equations of [P_{66614}][A] (A = TFSA, PFOS, and PF_6).

	TFSA	PFOS	PF_6
Quadratic equation			
a (kg·m^{-3})	1306.277	1473.098	1202.064
b (kg·m^{-3}·K^{-1})	−0.878	−1.035	−0.713
c (kg·m^{-3}·K^{-2})	2.562×10^{-4}	2.509×10^{-4}	1.029×10^{-4}
ARD of fit (%)	0.013	0.003	0.005
Arrhenius equation			
A (mPa·s)	3.708×10^{-5}	4.631×10^{-6}	4.310×10^{-5}
E_a (J·mol^{-1})	39822.709	48497.302	42509.996
ARD of fit (%)	1.781	1.024	0.180
VFT equation			
A (mPa·s)	2.589×10^{-2}	1.423×10^{-2}	4.874×10^{-4}
B (K)	1553.779	1749.198	3586.640
T_0 (K)	133.577	147.462	55.526
ARD of fit (%)	0.095	0.452	0.131

Table S10. Dependence of density ρ (kg·m^{-3}) on the pressure p (MPa) of [P_{66614}][A] (A = TFSA, PFOS, and PF_6). Standard uncertainties of temperature and pressure were 0.01 K and 1 kPa, respectively. Relative expanded uncertainty for density was 0.001 (average of 10 measurements).

p	ρ	p	ρ	p	ρ
T = 313.15 K					
TFSA		PFOS		PF_6	
0.094	1056.91	0.094	1174.57	0.103	991.16
1.001	1057.56	1.000	1175.44	1.000	991.71
2.001	1058.36	2.001	1176.34	2.000	992.28
4.000	1059.81	3.999	1178.22	4.000	993.42
5.999	1061.22	6.000	1180.09	6.000	994.67
8.000	1062.67	8.000	1181.87	8.000	995.85
9.999	1064.03	9.999	1183.66	10.001	997.05
20.001	1070.73	20.001	1192.10	20.001	1002.86
30.000	1077.08	29.999	1199.93	30.000	1008.52
39.999	1083.07	39.999	1207.29	40.001	1013.81
50.000	1088.80	50.001	1214.21	50.001	1018.85
T = 333.15 K					
TFSA		PFOS		PF_6	
0.100	1042.25	0.099	1156.79	0.105	977.56
1.000	1043.16	1.000	1157.73	1.001	978.18
2.000	1043.96	2.000	1158.77	2.001	978.86
4.000	1045.51	4.000	1160.84	4.000	980.24
6.001	1047.06	6.001	1162.86	6.001	981.59
7.999	1048.57	8.000	1164.82	8.001	982.90
10.000	1050.06	10.001	1166.79	10.000	984.19
20.001	1057.24	19.999	1175.95	20.000	990.51
30.001	1063.98	30.000	1184.47	30.000	996.44
40.000	1070.36	40.000	1192.42	40.001	1002.13
50.000	1076.42	49.999	1199.88	49.999	1007.53

Table S11. Coefficients of the best fits of the Tait and Sanchez–Lacombe equations for the high-pressure densities of $[P_{66614}][A]$ (A = TFSA, PFOS, and PF_6).

	TFSA	PFOS	PF_6
Tait Equation			
a_0 (kg·m^{-3})	1156.376	1314.128	1170.026
a_1 (kg·m^{-3}·K^{-1})	6.991×10^{-2}	-2.927×10^{-2}	-4.669×10^{-1}
a_2 (kg·m^{-3}·K^{-2})	-1.237×10^{-3}	-1.330×10^{-3}	-3.329×10^{-4}
b_0 (MPa)	568.572	589.265	677.361
b_1 (K^{-1})	4.658×10^{-3}	5.589×10^{-3}	4.553×10^{-3}
C (–)	9.112×10^{-2}	8.226×10^{-2}	1.022×10^{-1}
ARD of fit (%)	0.004	0.004	0.010
Sanchez–Lacombe Equation			
p^* (MPa)	339.886	327.899	382.873
ρ^* (kg·m^{-3})	1142.843	1282.998	1077.066
T^* (K)	616.341	589.517	604.982
M (–)	764.000	982.980	511.520
ARD of fit (%)	0.138	0.075	0.085

Supporting References

(1) Blundell, R. K.; Licence, P. Quaternary Ammonium and Phosphonium Based Ionic Liquids: A Comparison of Common Anions. *Phys. Chem. Chem. Phys.* **2014**, *16*, 15278–15288.

(2) Kang, C. S. M.; Zhang, X.; MacFarlane, D. R. Synthesis and Physicochemical Properties of Fluorinated Ionic Liquids with High Nitrogen Gas Solubility. *J. Phys. Chem. C* **2018**, *122*, 24550–24558.

(3) Kodama, D.; Kanakubo, M.; Kokubo, M.; Hashimoto, S.; Nanjo, H.; Kato, M. Density, Viscosity, and Solubility of Carbon Dioxide in Glymes. *Fluid Phase Equilib.* **2011**, *302*, 103–108.

(4) Kodama, D.; Sato, K.; Watanabe, M.; Sugawara, T.; Makino, T.; Kanakubo, M. Density, Viscosity, and CO_2 Solubility in the Ionic Liquid Mixtures of [bmim][PF_6] and [bmim][TFSA] at 313.15 K. *J. Chem. Eng. Data*. **2018**, *63*, 1036–1043.

(5) Watanabe, M.; Kodama, D.; Makino, T.; Kanakubo, M. Density, Viscosity, and Electrical Conductivity of Protic Amidium Bis(Trifluoromethanesulfonyl)Amide Ionic Liquids. *J. Chem. Eng. Data*. **2016**, *61*, 4215–4221.

(6) Harris, K. R.; Kanakubo, M.; Kodama, D.; Makino, T.; Mizuguchi, Y.; Watanabe, M.; Watanabe, T. Temperature and Density Dependence of the Transport Properties of the Ionic Liquid Triethylpentylphonium Bis(Trifluoromethanesulfonyl)Amide, [$P_{222,5}$][Tf_2N]. *J. Chem. Eng. Data*. **2018**, *63*, 2015–2027.

(7) May, E. F.; Tay, W. J.; Nania, M.; Aleji, A.; Al-Ghafri, S.; Trusler, J. P. Physical Apparatus Parameters and Model for Vibrating Tube Densimeters at Pressures to 140 MPa and Temperatures to 473 K. *Rev. Sci. Instrum.* **2014**, *85*, 095111.

(8) Nanda, V. S.; Simha, R. Equation of State of Polymer Liquids and Glasses at Elevated Pressures. *J. Chem. Phys.* **1964**, *41*, 3870–3878.

(9) Sanchez, I. C.; Lacombe, R. H. An Elementary Molecular Theory of Classical Fluids. Pure Fluids. *J. Phys. Chem.* **1976**, *80*, 2352–2362.

(10) Sanchez, I. C.; Lacombe, R. H. Statistical Thermodynamics of Polymer Solutions. *Macromolecules*. **1978**, *11*, 1145–1156.